Synthesis, Characterization, Photocatalysis, and Antibacterial Study of WO₃, MXene and WO₃/MXene Nanocomposite

Al-Zoha Warsi [1], Fatima Aziz [1], Sonia Zulfiqar [2], Sajjad Haider [3], Imran Shakir [4] and Philips O. Agboola [5,*]

[1] Baghdad-ul-Jadeed Campus, Institute of Chemistry, The Islamia University of Bahawalpur, Bahawalpur 63100, Pakistan; zohawarsi2208@gmail.com (A.-Z.W.); fatimaaziz408@gmail.com (F.A.)

[2] Department of Chemistry, School of Sciences & Engineering, The American University in Cairo, New Cairo 11835, Egypt; sonia.zulfiqar@aucegypt.edu

[3] Department of Chemical Engineering, College of Engineering, King Saud University, P.O. Box 800, Riyadh 11421, Saudi Arabia; shaider@ksu.edu.sa

[4] Sustainable Energy Technologies (SET) Center, College of Engineering, King Saud University, P.O. Box 800, Riyadh 11421, Saudi Arabia; mshakir@ksu.edu.sa

[5] College of Engineering, Al-Muzahmia Branch, King Saud University, P.O. Box 800, Riyadh 11421, Saudi Arabia

* Correspondence: pagboola@ksu.edu.sa

Abstract: Tungsten oxide (WO_3), MXene, and an WO_3/MXene nanocomposite were synthesized to study their photocatalytic and biological applications. Tungsten oxide was synthesized by an easy and cost-effective hydrothermal method, and its composite with MXene was prepared through the sonication method. The synthesized tungsten oxide, MXene, and its composite were characterized by X-ray diffraction (XRD), field emission scanning electron microscopy (FESEM), Fourier transform infrared (FTIR), energy-dispersive X-ray analysis (EDX), and Brunauer–Emmett–Teller (BET) for their structural, morphological, spectral, elemental and surface area analysis, respectively. The crystallite size of WO_3 calculated from XRD was ~10 nm, the particle size of WO_3 was 130 nm, and the average thickness of MXene layers was 175 nm, which was calculated from FESEM. The photocatalytic activity of as-synthesized samples was carried out for the degradation of methylene blue under solar radiation, MXene, the WO_3/MXene composite, and WO_3 exhibited 54%, 89%, and 99% photocatalytic degradation, respectively. WO_3 showed maximal degradation ability; by adding WO_3 to MXene, the degradation ability of MXene was enhanced. Studies on antibacterial activity demonstrated that these samples are good antibacterial agents against positive strains, and their antibacterial activity against negative strains depends upon their concentration. Against positive strains, the WO_3/MXene composite's inhibition zone was at 7 mm, while it became 9 mm upon increasing the concentration. This study proves that WO_3, MXene, and the WO_3/MXene nanocomposite could be used in biological and environmental applications.

Keywords: WO_3; MXene; XRD; FESEM; EDX; photocatalysis

1. Introduction

In the last few decades, environmental remediation technologies have been the most challenging for effective and efficient water cleaning, primarily through the photocatalytic method [1–6]. Such catalysts are cost-effective and have a suitable energy and electronic structure. Minimal amounts of contaminants such as phenols, textile dyes, and poly chlorinated biphenyls (PCBs) not only pollute the water, but also reduce the growth of aqueous organisms [7]. For the removal of such pollutants from water, various physical and chemical methods were reported [8,9]. However, these methods are either expensive or suitable for large amounts of contaminants [10]. So, the photocatalytic degradation of organic contaminants has gained much attention due to its efficiency and cost-effectiveness [7,11].

Owing to their surface, electronic and crystal structure, various semiconductors, mainly metal oxides such as ZnO, TiO_2, Fe_2O_3 and WO_3, and sulfides (ZnS, CdS) showed

exceptional photocatalytic behavior [10,12,13]. Among all of these metal oxides, TiO_2 exhibited good photostability and photocatalytic activity in an aqueous medium [14,15]. However, due to its high charge recombination and wide band gap, its applications are restricted [16]. Meanwhile, Fe_2O_3 and ZnO are quite unstable in wastewater at various pH values, which limits its applications [10]. Sulfide-based catalysts are also not suitable for water remediation because they release toxic sulfides on illumination [10]. Among several metal oxides, WO_3 is a more appropriate candidate for photocatalytic degradation owing to its abundance and narrow band gap, physical and chemical stability, and photosensitivity in visible-light area [17]. Among major global problems, cancer is the most important, and scientists are striving to solve it [18,19]. Recently, they succeeded in tracking cancer using tungsten oxide in mice [20]. So, the preparation of tungsten oxide is quite interesting. So far, various technologies have been used and reported for the synthesis of tungsten oxide, such as hydrothermal method, acid precipitation, and sol-gel [21–27]. By controlling the reaction time, precursor material, hydrothermal temperature, and capping agents, the optical properties, crystallinity, and morphology of WO_3 nanostructures can be varied. MXene, an emerging 2D material, is a layered structured transition metal, nitride or carbide, having both a hydrophilic nature and high electrical conductivity. They have large interlayer spacing, a greater surface area, and a large number of active surface sites [28]. They can also sequester and remove dyes, heavy metals, and radioactive nuclides [29].

MXene is a potential candidate for the synthesis of electrode material for various energy storage devices such as supercapacitors and batteries. Metal-oxide- and metal-sulfide-based composites were reported to be better electrode materials for supercapacitor electrodes [30–38]. Therefore, MXene-based composites were also explored for better properties [39,40]. The capacitance of MXene-based devices can be further enhanced by producing its composites with other materials such as reduced graphene oxide, metal oxides, and conducting polymers [41,42]. Scientists are also attempting to use certain pristine metal oxides and their composites with 2D materials in various biological applications [43–47].

The main goal behind this research is to develop a unique WO_3/MXene composite that exhibits potential applications in biological and environmental remediation. In this paper, MXene was synthesized by etching an Al atomic layer from MAX powder. The hydrothermal route was used to synthesize tungsten oxide nanorods. The WO_3/MXene composite was synthesized by a simple sonication method. These prepared samples were characterized for structural, spectral, morphological, and elemental analyses. The photocatalytic and antibacterial activity of the as-synthesized samples was measured and is discussed in detail.

2. Experimental Work

2.1. Materials

MAX powder (Ti_3AlC_2) (98% purity); hydrofluoric acid (HF) (40 wt %, Merck, Darmstadt, Germany); deionized (DI) water; sodium tungstate ($Na_2WO_4.2H_2O$, 99%, Sigma-Aldrich, Burlington, MA, USA), sodium sulfate (Na_2SO_4, 99%, Sigma-Aldrich, Burlington, MA, USA), HCl (36%, Fischer Scientific, Waltham, MA, USA).

2.2. Synthesis of MXene

MAX powder (Ti_3AlC_2) was used to prepare the MXene with the $Ti_3C_2T_x$ formula in a 50 mL Teflon vessel. For this purpose, Al was etched by using an HF solution. For the preparation of MXene, 10 mL HF was poured inside the Teflon vessel and then placed in a fume hood. Then, 0.5 g of MAX powder was slowly added into the HF solution pinch by pinch. Then, the whole mixture was stirred magnetically at room temperature for about 24 h for maximal etching. DI water was added to the resultant product for dilution, and multilayered MXene was obtained by centrifugation at 5000 rpm. The washing of these precipitates was repeated continuously until its pH became 6. The vacuum filtration of the aqueous dispersion was carried out by using a PTFE membrane. The filtrate containing

$Ti_3C_2T_x$ was then freeze-dried for 24 h. Schematic illustration for preparation of MXene is shown in Figure 1.
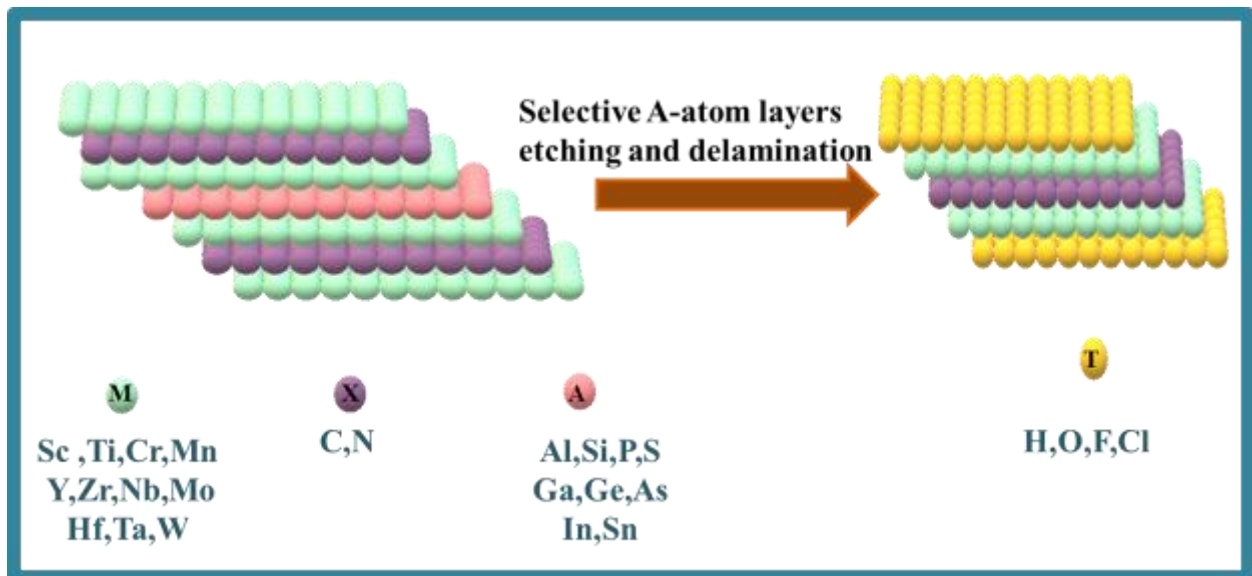
Figure 1. Structural representation of MXene.

### 2.3. Synthesis of Tungsten Oxide (WO_3)

2.5 g of sodium tungstate and 3.0 g of sodium sulfate were dissolved in 80 mL of distilled water. A 3M HCl solution was added dropwise to the clear solution under continuous stirring, and the pH of the solution was set to 1.5. After 10 min of stirring, the mixture was transferred into a Teflon-lined stainless-steel autoclave and was kept at 180 °C for 48 h. After that, the product was collected by centrifugation at 4500 rpm, and washed with distilled water and ethanol to obtain neutral solution; then, the product was obtained by drying at 60 °C in air.

2.4. Synthesis of WO_3/MXene Composites

The composite of WO_3/MXene (1:1) was fabricated by sonication method. Then, 2 g of MXene was added in 50 mL of water and sonicated for 3 h. Afterwards, 2 g of tungsten oxide was added to it, again sonicated for 2 h, and then dried in an oven. Synthesis of WO_3 and WO_3/MXene composites is shown in Figure 2.

2.5. Characterization

An XRD diffractometer using Cu Kα radiation (λ = 1.54 Å) as a light source, at a scan rate of 30 min by applying a voltage of 40 kV, was used for the structural and phase analysis of the as-synthesized samples. ZEISS LEO SUPRA 55 field emission scanning electron microscope and JEOL JCM-6000Plus SEM were used for morphological characterization and elemental analysis, respectively. Functional group analysis and the surface properties of the as-synthesized samples were measured by Fourier transform infrared spectroscopy (FTIR). For the measurement of the BET surface areas, nitrogen adsorption–desorption was conducted by flowing liquid nitrogen at 77 K (−196 °C) by using the Micromeritics ASAP 2020 Physisorption analyzer.
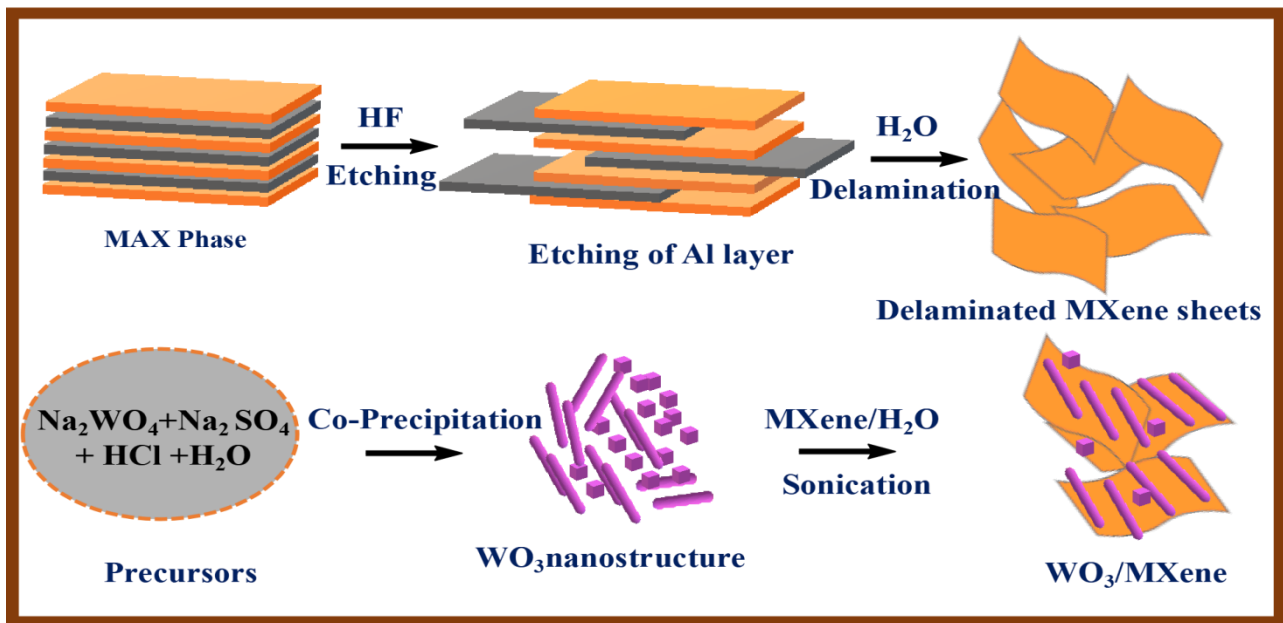
Figure 2. Schematic illustration summarizing synthesis of MXene, WO$_3$, and WO$_3$/MXene nanocomposite.

2.6. Photocatalytic Degradation

WO$_3$, MXene, and the WO$_3$/MXene nanocomposite were used as a photocatalyst to measure the photocatalytic degradation of methylene blue in the presence of solar radiation for 80 min. For these measurements, 100 mL of 5 ppm methylene blue solution was poured in a beaker, and 5 mg of photocatalyst was added into the solution. It was then stirred continuously for 60 min in the dark. Adsorption–desorption equilibrium could thus be achieved between methylene blue and photocatalyst. The solution was then placed in solar light with constant stirring. In order to measure the degradation percentage of methylene blue, 5 mL of a solution containing both dye and sample was taken after every 10 min, and a UV–vis spectrophotometer was used to measure the degradation efficiency of the samples [5,48].

The degradation percentage of the as-synthesized samples was measured by using following equation:

$$\%degradation = \frac{(C_0 - C_t)}{C_0} \times 100 \qquad (1)$$

where, C_t is the concentration of the solution at time t, and C_0 is the concentration of the solution at time zero.

2.7. Antibacterial Activity

The disc diffusion method was utilized to study the antibacterial activity of WO$_3$, MXene, and WO$_3$/MXene nanocomposite. *Staphylococcus aureus* (*S. aureus*) was used as a positive strain, and *Escherichia coli* (*E. coli*), *Klebsiella pneumonia* (*K. pneumonia*) and *Proteus vulgaris* (*P. vulgaris*) were used as negative strains. For standard/positive control, an antimicrobial agent (ciprofloxacin) was used. First, the aqueous solution of the as-prepared samples was prepared by sonicating the samples with distilled water. Then, they were placed on the corners of a nutrient agar plate with the use of forceps. After incubating the samples for 24 h at 37 °C, the zone of inhibition could be seen on the edges of the agar plate. The formation of these zones of inhibition confirmed the antibacterial activity, while the lack of these zones of inhibition showed no antibacterial activity. The mm units were used for the measurement of these inhibition zones.

3. Results and Discussion

3.1. XRD

The different phases of the as-fabricated WO_3, MXene, and their composite (WO_3/MXene) were studied by utilizing the Cu Kα radiation (λ = 1.5406 Å) with an X-ray diffractometer. Figure 3 shows the X-ray diffractograms. Tungsten oxide (WO_3) produced the diffraction peaks at 2 theta values 23°, 26°, 33°, 41°, 49° and 55°. The Miller indices corresponding to these peaks are (001), (101), (111), (110), (220) and (202) [49,50]. At 2θ = 23°, tungsten oxide ($WO_{2.95}$) gave a characteristic peak. For WO_3, peaks were more prominent at 2θ = 26°, corresponding to the Miller indices (111) [51]. The structure of the as-prepared WO_3 nanoparticles was compared with JCPDS card 00-002-0310.
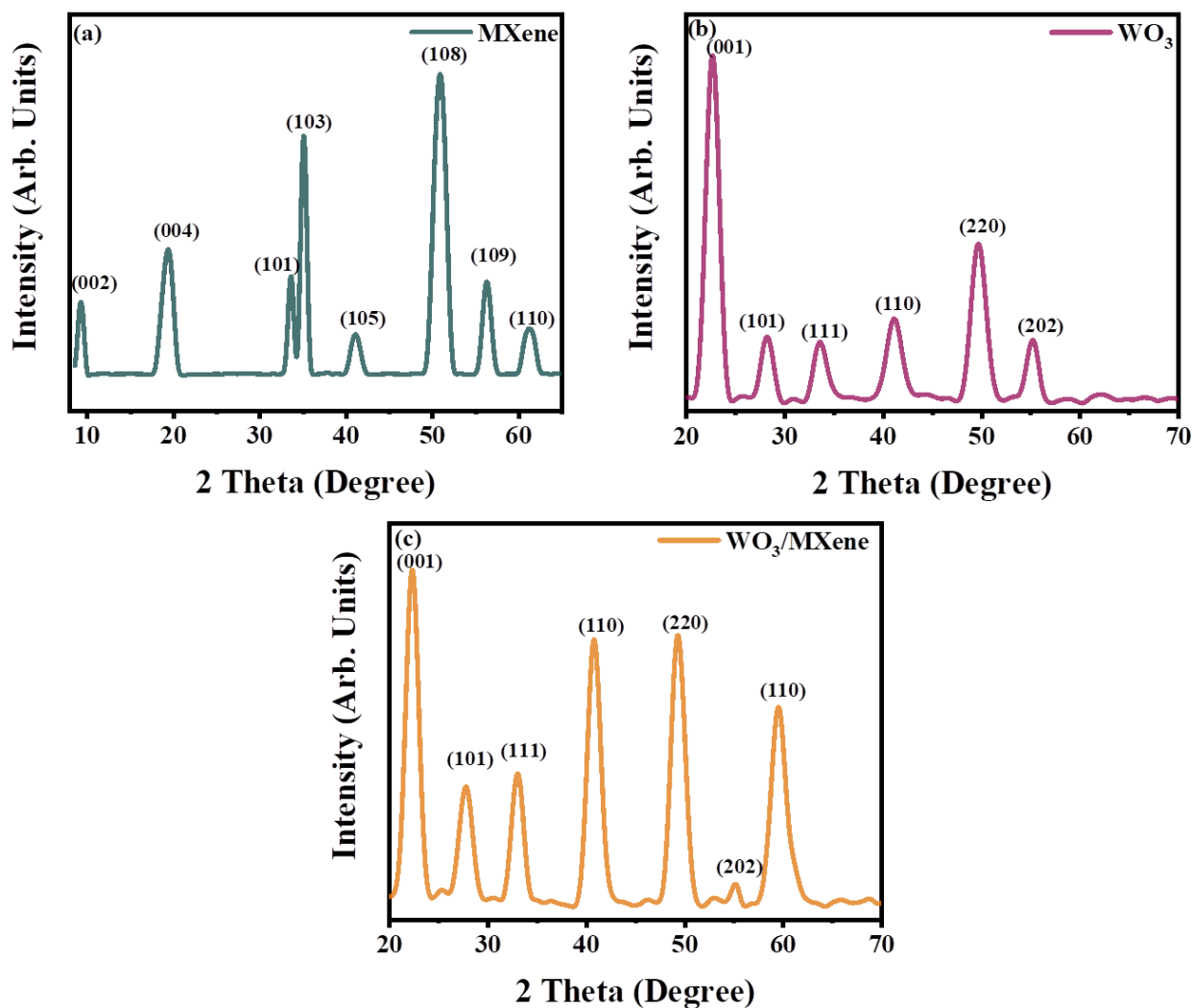

Figure 3. XRD spectra of (**a**) MXene, (**b**) WO_3, and (**c**) WO_3/MXene nanocomposite.

The pure MAX XRD pattern showed 2θ peaks at 9.11°, 18.7°, 33.58°, 35.65°, 38.61°, 41.44°, 51.93°, 56.08°, and 60.23°, which corresponds to Miller indices (002), (004), (101), (103), (104), (105), (108), (109), and (110), respectively [52,53]. Due to the presence of the Al, the pure MAX powder showed a characteristic peak at 2θ = 38.61°, which corresponds to (104). Al was completely etched by using HF in order to fabricate good-quality MXene [54,55]. During the first 2 h of the reaction, the peak intensity at 38.61° increased [56]. After 24 h of the reaction, the characteristic peak of MAX at (104) vanished, as shown in Figure 3a. A peak shift was also observed in the peak at 9.11° [57].

The XRD pattern was used for studying the phases of the composite (WO_3/MXene). Figure 3c shows the XRD pattern of the composite (WO_3/MXene), which possessed diffraction peaks at 23°, 26°, 33°, 41°, 49°, 55° and 60.23° corresponding to Miller indices (001), (101), (111), (110), (220), (202) and (110), respectively. All these peaks included almost all the specific peaks of tungsten and MXene, and no additional peak was observed in the case of composite.
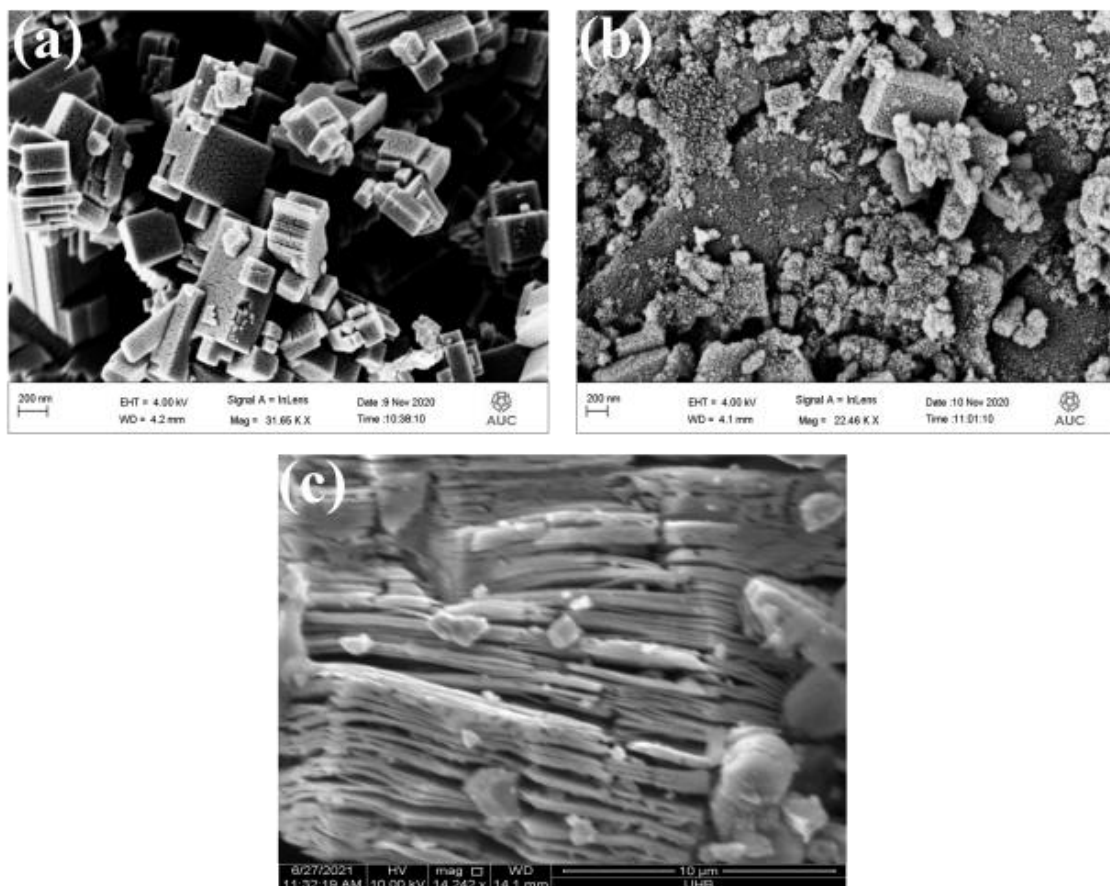
By using the Debye–Scherer equation, the crystallite size of the as-fabricated tungsten oxide was calculated [58].

$$D = K\lambda / \beta Cos\theta \tag{2}$$

where D is the crystalline size; K is the Scherer constant; λ is the X-ray wavelength of the copper source used in XRD, which was equal to 1.5406 Å; Bragg's angle was given by θ; and β represents full width at half maximum (FWHM) [59]. The crystalline size of WO_3 nanoparticles, determined by XRD, was 6.19 nm. The measurement of the crystalline size of MXene was not possible by using the Debye–Scherer formula because MXene is a 2D layered material.

3.2. FESEM and EDX Analysis

For FESEM analysis, the samples were gold-sputtered for 120 s at 15 mA before imaging. Figure 4a,b show the morphology of WO_3 and WO_3/MXene nanocomposite, respectively. Figure 4a demonstrates the block-/rodlike morphology of WO_3. Figure 4b clearly shows that MXene was impregnated on the nanorods of WO_3. The nanosheet-like structure in Figure 4c represents the formation of MXene. The particle size of WO_3 was ~130 nm, which was calculated from the FESEM image. The average layer thickness of MXene calculated from micrograph was ~175 nm.

Figure 4. FESEM images of (**a**) WO_3, (**b**) WO_3/MXene nanocomposite and (**c**) MXene.

Energy-dispersive X-ray analysis (EDX) was used for the elemental analysis of the synthesized material. Figure 5a,b show the elemental composition of WO_3 and WO_3/MXene composites, respectively, which confirmed the purity of the as-synthesized samples.

Figure 5. EDX analysis of (**a**) WO_3 and (**b**) WO_3/MXene nanocomposite.

3.3. FTIR

FTIR spectroscopy was used for the spectral analysis of the samples, which indicates the composition of synthesized products. Figure 6 shows the FTIR spectra of MXene, WO_3 and WO_3/MXene nanocomposite. In the case of MXene, the absorption band present at around 3545 cm^{-1} was attributed to the absorbed water, which was due to the hydrophilic nature of MXene [60]. The bands present in the range of 2000–2500 cm^{-1} showed a methyl/methylene group (–CH_3, CH_2). The signals at 603 and 1529 cm^{-1} were characteristic of Ti–O and C–F, respectively. The FTIR spectrum of WO_3 featured characteristics bands of W–O–W and W–O at around 735 and 836 cm^{-1} [49]. The spectrum of the WO_3/MXene nanocomposite showed the absorption bands of both MXene and WO_3.

Figure 6. FTIR spectra of MXene, WO_3, and WO_3/MXene nanocomposite.

3.4. BET Measurements

Average particle size, BET surface area, total pore volume, and average pore width were determined from nitrogen adsorption-desorption curves (Figure 7) and their values are given in Table 1. From the BET results, it was predicted that the formation of the composite of WO_3 with MXene would result in increased surface area and enhanced average pore width, while average particle size was reduced. The reason behind this is the 2D layer structure of MXene, which offers a greater surface area. However, the photocatalytic activity of WO_3 was higher than that of the composite because MXene only enhanced the surface area, but this increased surface area had no effect on the degradation of dyes because the adsorption capacity and band gap of MXene were much less, due to which charge separation was not effective.
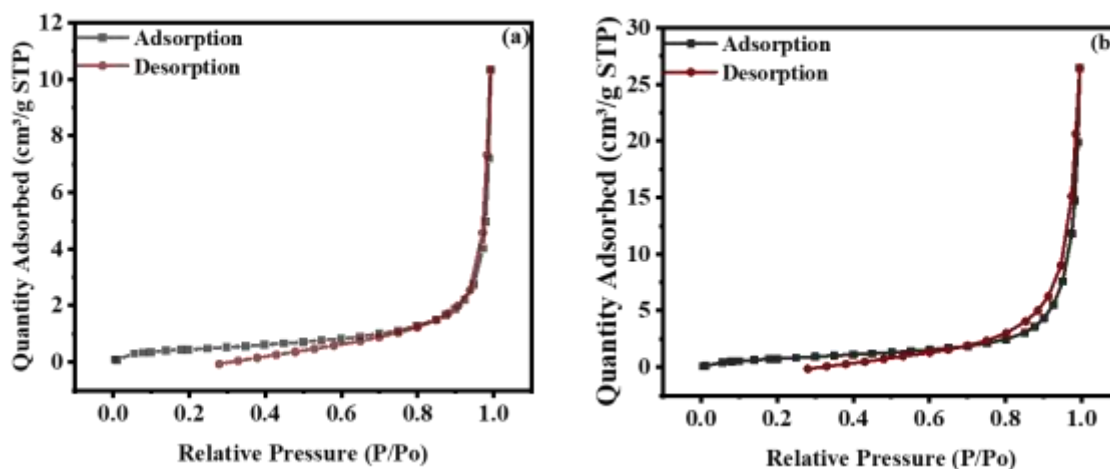

Figure 7. Nitrogen adsorption–desorption isotherm of (**a**) WO_3 and (**b**) WO_3/MXene nanocomposite.

Table 1. Surface properties of WO_3, WO_3/MXene nanocomposite calculated from BET analysis.

S. No.	Properties	WO_3	WO_3/MXene Nanocomposite
1	BET surface area	1.63 m^2/g	3.15 m^2/g
2	Average particle size	3. 6 µm	1.9 µm
3	Total adsorption pore volume	0.0111 cm^3/g	0.0307 cm^3/g
4	Average pore width	27.3 nm	39 nm

3.5. Photocatalysis

The photocatalytic activity of WO_3, MXene, and the WO_3/MXene nanocomposite was measured for the degradation of methylene blue under solar radiation for 80 min. The initial concentration of methylene blue was determined by measuring the blank absorption of the dye solution. For the achievement of adsorption–desorption equilibrium between photocatalyst and methylene blue, the solution was placed in the dark for 1 h with continuous stirring. The solution containing both methylene blue and sample was then kept under solar radiation. By taking 5 mL solution after regular intervals, the degradation of the dye was measured by using a UV–vis spectrophotometer [61].

The absorption spectra of methylene blue using WO_3, MXene, and the WO_3/MXene nanocomposite as photocatalyst are shown in Figure 8a–c). For the description of the experimental data given in Figure 9, a pseudo-first-order model was utilized, and the values of K measured by this model were 0.05682, −0.0084, and 0.0346 for WO_3, MXene, and the WO_3/MXene nanocomposite, respectively.

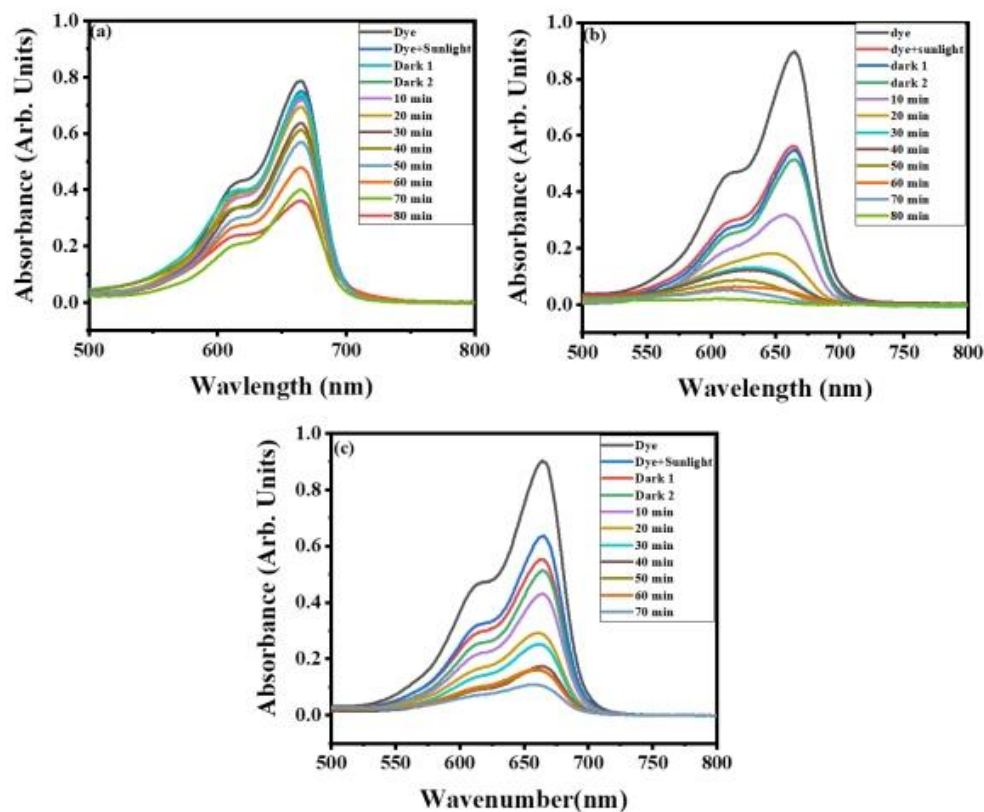**Figure 8.** Absorption spectra for photocatalytic degradation of methylene blue by (**a**) MXene, (**b**) WO$_3$, and (**c**) WO$_3$/MXene nanocomposite.
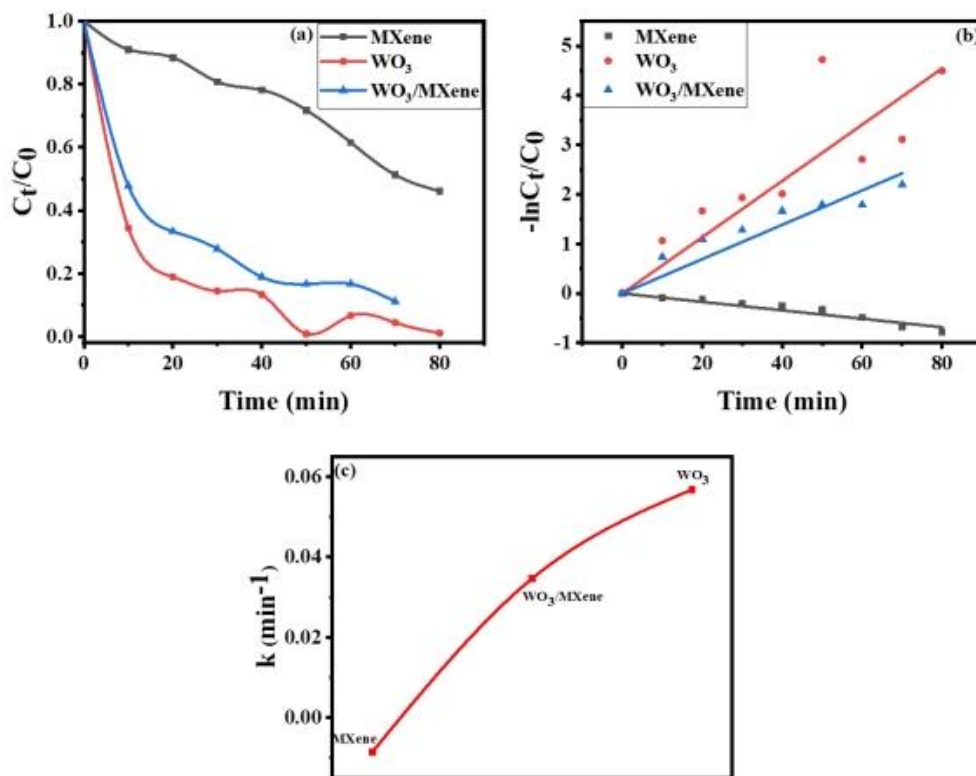

Figure 9. (**a**–**c**) Kinetic study for rate constant of MXene, WO$_3$, and WO$_3$/MXene nanocomposite.

Figure 10 demonstrates the removal efficiency of WO$_3$, MXene, and the WO$_3$/MXene nanocomposite. WO$_3$ showed higher degradation ability as compared to that of MXene

and the WO_3/MXene composite. The reason behind this high photocatalytic activity is the greater band gap of WO_3, which allowed for them to absorb a wide-spectrum range of sunlight and degrade the dye solution with this solar energy. MXene exhibited very low removal efficiency, while the degradation ability of WO_3/MXene composite was between those of WO_3 and MXene. MXene is a 2D material that acts as a supporting material. WO_3 is material that involves the generation of photo produced electrons and holes. MXene merely increases the surface area and reduces the chances of recombination of these photogenerated electrons and holes. Figure 11 shows the comparison of the degradation percentage of methylene blue by WO_3, MXene, and the WO_3/MXene nanocomposite.

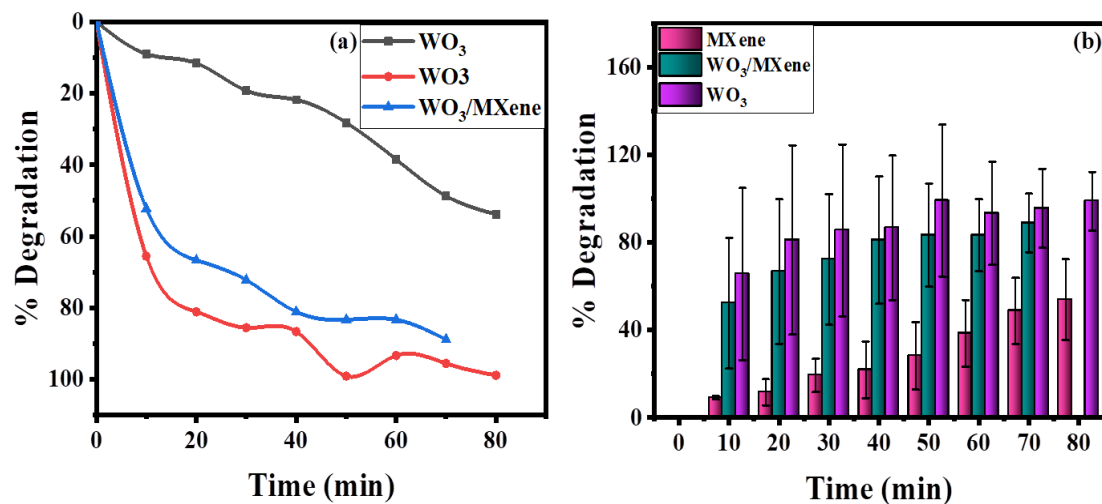**Figure 10.** (**a**) Comparison of photocatalytic degradation of methylene blue by WO_3, MXene, and WO_3/Mxene (**b**) bar chart representation of percentage degradation with error bars.

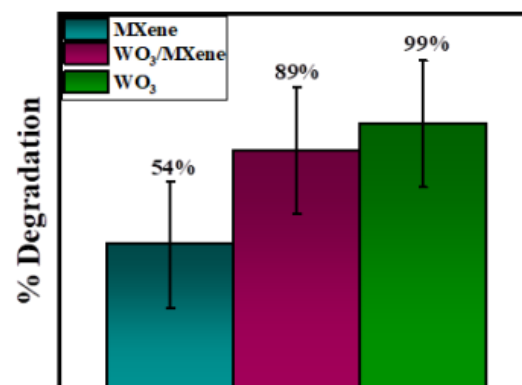**Figure 11.** Comparison of degradation percentage of methylene blue using WO_3, MXene, and WO_3/MXene nanocomposite.

Mechanism

An emerging degradation technology that leads to the removal of most contaminants is heterogeneous photocatalysis [44]. The comparison of current reported catalysts with already reported similar materials is given in Table 2.

Table 2. Comparison between the degradation percentage of the current research with values reported in the literature.

Sr. No.	Photocatalyst	Pollutant	Light Source	% Degradation	Time (min)	Reference
1.	ZnO/Ag	Methyl orange	Visible light	78%	180	[62]
2.	NiO/Ag	Methyl orange	Visible light	42%	180	[62]
3.	TiO_2/Ag	Methyl orange	Visible light	86%	180	[62]
4.	AgO	Methyl orange	Visible light	60.5%	50	[63]
5.	CoO	Methyl orange	Visible light	71.24%	50	[63]
6.	CdO	Methyl orange	Visible light	80.2%	50	[63]
7.	AgO–CoO–CdO/PACSGO	Methyl orange	Visible light	97.4%	50	[63]
8.	CdO	Methylene blue	Sunlight	78%	–	[64]
9.	CdO	Congo red	Sunlight	81%	–	[65]
10.	SnO_2	Congo red	Sunlight	90%	–	[66]
11.	CdO	Alizarin red S	Sunlight	78%	–	[67]
12.	MgO	Alizarin red S	Sunlight	70%	–	[67]
13.	ZrO_2	Methylene blue	UV-light	99%	–	[68]
14.	MgO	Methylene blue	Sunlight	88%	–	[69]
15.	NiO	Evans blue	Sunlight	88.13%	–	[70]
17.	CdO–NiO–ZnO	Methylene blue	Sunlight	89%	–	[71]
18.	CdO–ZnO–MgO	Methylene blue	Sunlight	91%	–	[72]
19.	CdO–MgO	Alizarin red S	Sunlight	82%	–	[73]
20.	WO_3	Methylene blue	Sunlight	99%	80	Current Work
21.	WO_3/MXene	Methylene blue	Sunlight	89%	70	Current Work
22.	MXene	Methylene blue	Sunlight	54%	80	Current Work

The proposed mechanism involved in photocatalytic degradation consists of the following steps [74] and also depicted in Figure 12:
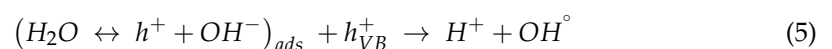
1. Efficient photons from sunlight are absorbed by WO_3:

$$(WO_3) + h\upsilon \; \rightarrow \; e^-_{CB} + h^+_{VB} \tag{3}$$

2. Ion sorption of oxygen takes place (start of oxygen reduction where the oxidation state of oxygen changes from 0 to $-1/2$).

$$(O_2)_{ads} + e^-_{CB} \; \rightarrow \; O^{\cdot-}_2 \tag{4}$$
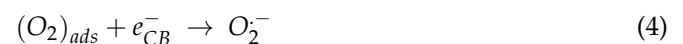
3. Photogenerated holes neutralize the $–OH$ group and produce $OH°$ radicals.

$$\left(H_2O \; \leftrightarrow \; h^+ + OH^- \right)_{ads} + h^+_{VB} \; \rightarrow \; H^+ + OH^\circ \tag{5}$$

4. Protons neutralize the $O^{\circ-}_2$

$$O^{\circ-}_2 + H^+ \; \rightarrow \; HO^\circ_2 \tag{6}$$

5. Dismutation of oxygen occurs, and transient H_2O_2 is formed:

$$2HO_2^{\circ -} \;\rightarrow\; H_2O_2 + O_2 \tag{7}$$

6. Oxygen is reduced for the second time, and the decomposition of H_2O_2 occurs:

$$H_2O_2 + e^- \;\rightarrow\; OH^\circ + OH^- \tag{8}$$

7. OH° radical attacks the organic pollutant (*dye*) and ultimately causes its oxidation:

$$Dye + OH^\circ \;\rightarrow\; Dye^\circ + H_2O \tag{9}$$

8. Direct oxidation takes place when it reacts with holes:

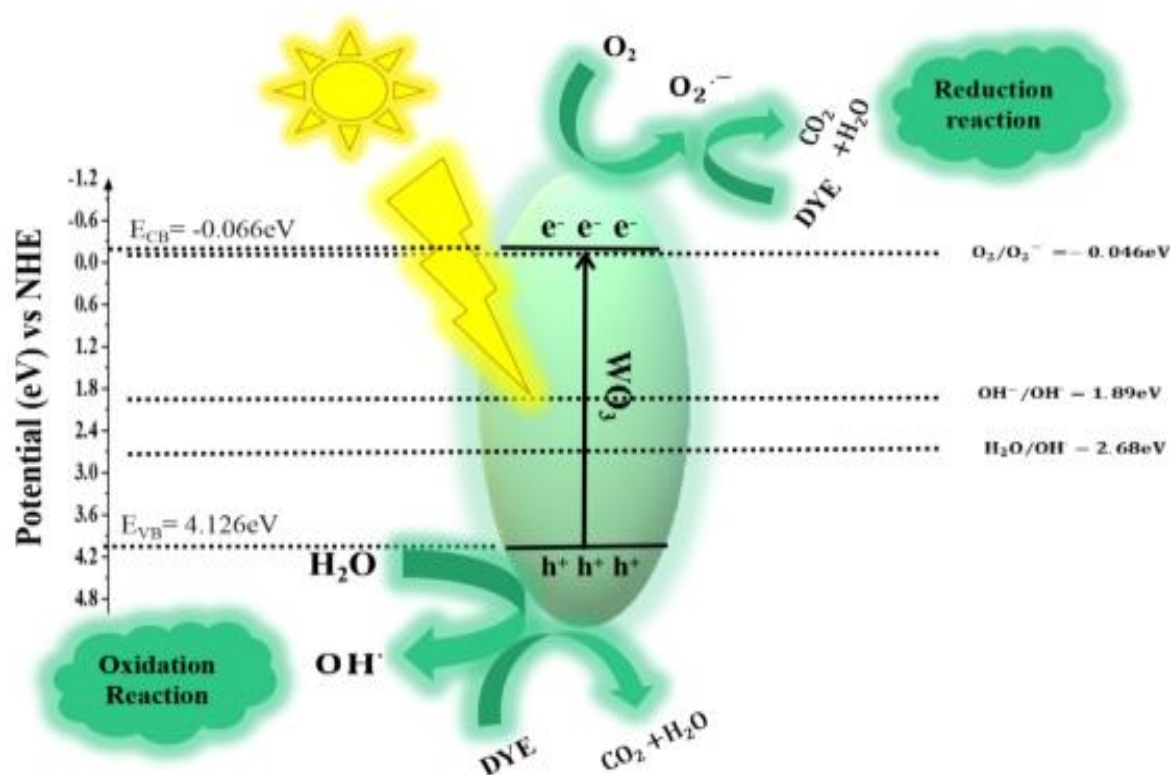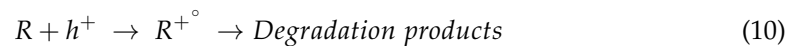$$R + h^+ \;\rightarrow\; R^{+\circ} \;\rightarrow\; Degradation\ products \tag{10}$$

Figure 12. Z-scheme mechanism for the photocatalytic activity of WO$_3$.

3.6. Antibacterial Activity

Among metal oxide nanoparticles, ZnO is a competitive candidate for the study of antibacterial activity. Recent studies showed that ZnO nanoparticles could activate endoplasmic reticulum stress and ultimately kill mammalian cells [75]. Therefore, scientists have been striving to explore new nano-antibacterial agents with better compatibility. Recently, WO$_{3-x}$ was verified to exhibit good biocompatibility and antibacterial activity [76]. In the current study, WO$_3$, MXene, and the WO$_3$/MXene nanocomposite were used as antibacterial agents for the study of antibacterial activity (Figures 13–16). Table 3 shows the zones of inhibition of WO$_3$, MXene, and the WO$_3$/MXene nanocomposite. The disc diffusion method was utilized to measure the inhibition zones of the as-prepared samples, and various positive strains (*S. aureus*) and negative strains *E. coli*, *K. pneumonia* and *P. vulgaris* were used for antibacterial activity measurements. Due to the structural differences of cell membranes and cell walls, the as-synthesized samples exhibited different sensitivity levels towards the positive and negative strains [77,78]. Table 3 shows that, with the positive strain (*S. aureus*), all samples showed good antibacterial activity, which

increased with the increase in concentration. In the case of negative strains, all samples were active against *K. pneumoniae*, and the WO$_3$/MXene composite showed good activity at a low concentration. When the concentration of MXene and WO$_3$ increased, activity also increased. The WO$_3$/MXene nanocomposite showed no activity against *E. coli* and *P. vulgaris*, while WO$_3$ and MXene exhibited good antibacterial activity, which was enhanced on the increase in concentration. The reason behind the low or zero antibacterial activity of the WO$_3$/MXene composite against negative strains was the presence of an extra outer membrane that increased the resistance of Gram-negative strains to WO$_3$/MXene. The WO$_3$/MXene nanocomposite showed a decrease in antibacterial activity on an increase in concentration due to certain factors such as size and agglomeration. Due to these factors, these nanocomposites were not able to penetrate the bacterial cell wall; hence, its toxicity decreased. On the other hand, the pristine WO$_3$ and MXene showed an increase in antibacterial activity on increasing concentration.
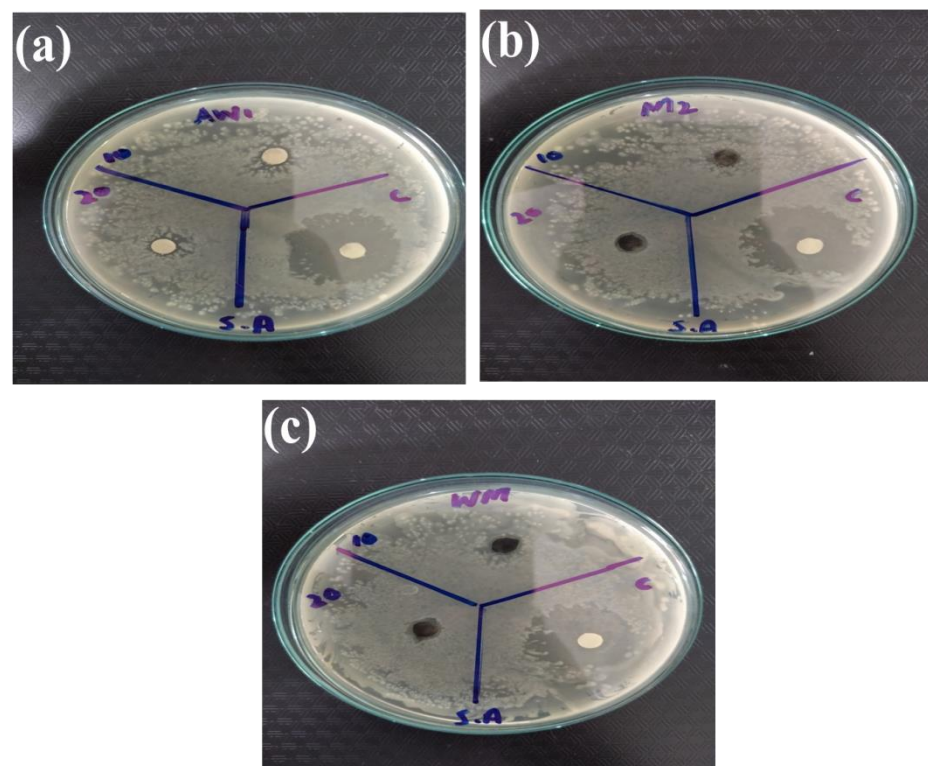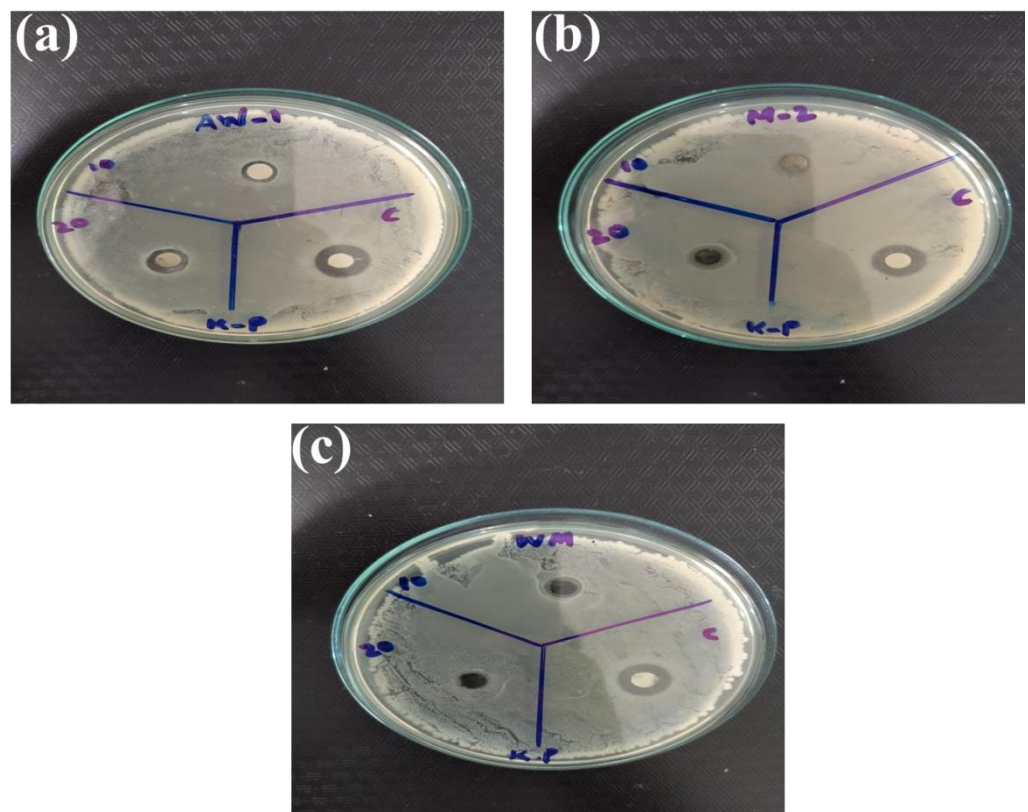

Figure 13. Antibacterial activity of (**a**) WO$_3$, (**b**) Mxene and (**c**) WO$_3$/Mxene against *Staphylococcus aureus*.

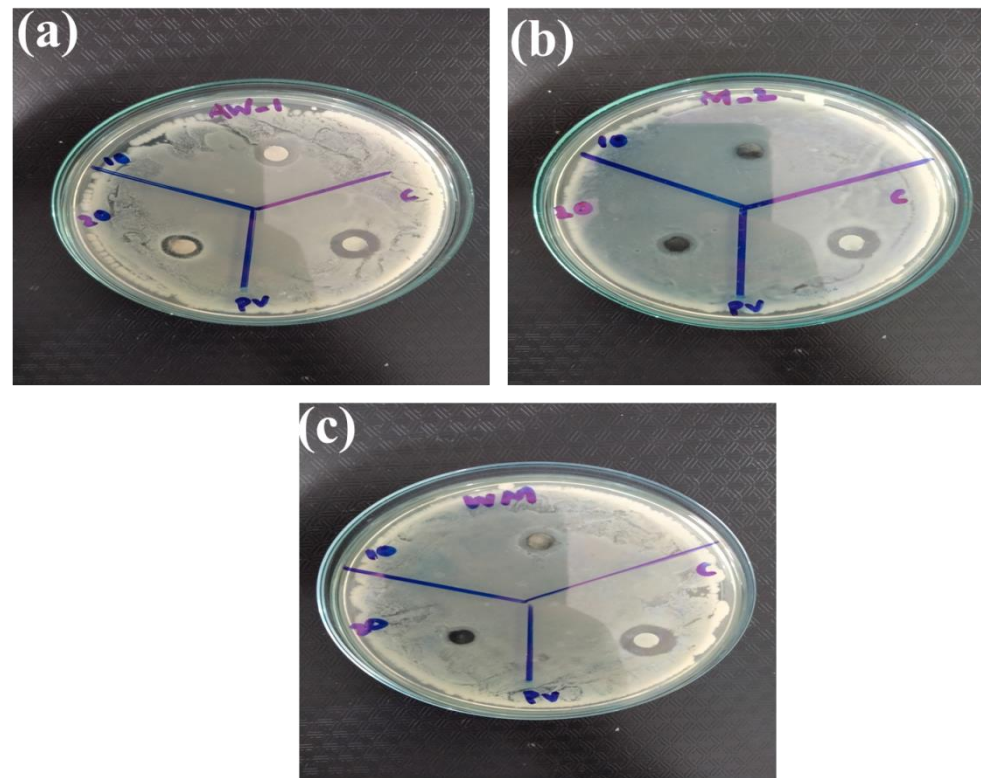**Table 3.** Results of antibacterial activity of as-synthesized samples.

Sr. No.	Sample	Concentration	*S. aureus*	*K. pneumoniae*	*E. coli*	*P. vulgaris*
1.	WO$_3$/MXene	10 mg/mL	07 mm	08 mm	00 mm	00 mm
		20 mg/m	09 mm	00 mm	00 mm	00 mm
	Ciprofloxacin	10 ug/mL	22 mm	12 mm	12 mm	13 mm
2.	MXene	10 mg/mL	00 mm	00 mm	08 mm	00 mm
		20 mg/m	08 mm	10 mm	08 mm	10 mm
	Ciprofloxacin	10 ug/mL	22 mm	12 mm	12 mm	13 mm
3.	WO$_3$	10 mg/mL	07 mm	07 mm	06 mm	00 mm
		20 mg/m	07 mm	10 mm	07 mm	11 mm
	Ciprofloxacin	10 ug/mL	22 mm	12 mm	12 mm	13 mm
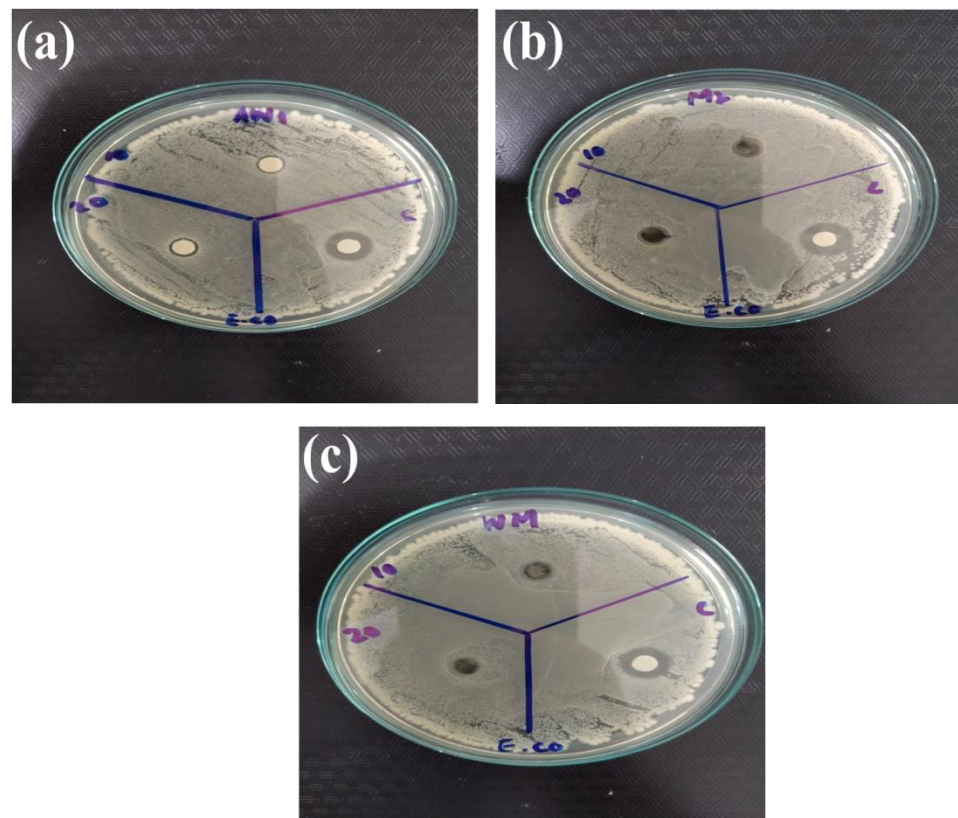
Figure 14. Antibacterial activity of as-prepared samples (**a**) WO$_3$, (**b**) Mxene and (**c**) WO$_3$/Mxene against *Escherichia coli (E. coli)*.

Figure 15. Antibacterial activity of as-prepared material (**a**) WO$_3$, (**b**) Mxene and (**c**) WO$_3$/Mxene against *Klebsiella pneumonia (K. pneumonia)*.

Figure 16. Antibacterial activity of as prepared materials (**a**) WO$_3$, (**b**) Mxene and (**c**) WO$_3$/Mxene against *Proteus vulgaris (P. vulgaris)*.

3.7. Mechanism of Antibacterial Activity

The mechanism involved with the antibacterial activity of the as-synthesized nanoparticles was the cell damage by electrostatic interactions between the cell membrane and metal oxide nanoparticles. The main sites of attraction of metal cations are the chemical groups of polymers on membranes of bacteria that are electronegative in nature. The carboxylic groups present in the proteins are the main reason behind the negative charge on the surface of bacteria. Electrostatic attraction is created due to the charge difference between bacterial membrane and metal oxide nanoparticles; thus, these nanoparticles accumulated on the cell surface and ultimately entered the bacteria. This interaction between membrane polymer and cationic metal oxide nanoparticles resulted in the cytoxicity of microorganisms. The available surface area and ratio of particle size to surface area determine the efficiency of metal oxide nanoparticles in bacterial growth inhibition. The permeability and structure of the cell membrane are changed due to the attachment of metal oxide nanoparticles. The disorganization of cell wall was due to the strong bond between positively charged metal oxide nanoparticles and membrane. Apart from binding with the cell membrane, these metal oxide nanoparticles also bind with mesosomes, resulting in the alteration of cell division, DNA replication, and cellular respiration [79].

4. Conclusions

In the current work, we prepared WO$_3$, MXene, and a WO$_3$/MXene nanocomposite, which exhibited their potential applications in the biological and environmental remediation fields. WO$_3$, MXene, and the WO$_3$/MXene nanocomposite were synthesized by hydrothermal method, wet chemical etching, and sonication method, respectively. XRD, FTIR, EDX, and FESEM were used to characterize the as-synthesized samples for structural, spectral, elemental, and morphological analysis, respectively. BET analysis was conducted for surface area determination. The photocatalytic degradation of methylene blue using WO$_3$, MXene, and the WO$_3$/MXene nanocomposite was 99%, 54%, and 89%,

respectively. The photocatalytic activity of WO_3 was significant. MXene is a 2D material, its photocatalytic activity is very low, and it only acted as supporting material by enhancing the photocatalytic ability of its composite with WO_3. The as-prepared samples also exhibited good antibacterial activity against positive strain bacteria; in the case of negative strains, WO_3, MXene, and the WO_3/MXene nanocomposite exhibited antibacterial activity at high concentrations.

Author Contributions: Conceptualization, I.S.; methodology, F.A.; software, S.Z.; validation, S.H.; formal analysis, A.-Z.W.; data curation, S.Z.; writing—original draft preparation, A.-Z.W.; writing— review and editing, S.H.; supervision, I.S.; project administration, P.O.A.; funding acquisition, P.O.A. All authors have read and agreed to the published version of the manuscript.

Conflicts of Interest: The authors declare no conflict of interest.

References

1. Chong, M.N.; Jin, B.; Chow, C.W.K.; Saint, C. Recent developments in photocatalytic water treatment technology: A review. *Water Res.* **2010**, *44*, 2997–3027. [CrossRef] [PubMed]
2. Legrini, O.; Oliveros, E.; Braun, A.M. Photochemical processes for water treatment. *Chem. Rev.* **1993**, *93*, 671–698. [CrossRef]
3. Daud, A.; Warsi, M.F.; Zulfiqar, S.; Agboola, P.O.; Rehman, A.-U.; Shakir, I. Fabrication of $GdFO_3$-Carbon nanotubes nanocomposites for enhanced photocatalytic applications. *Ceram. Int.* **2020**, *46*, 12884–12890. [CrossRef]
4. Irshad, A.; Warsi, M.F.; Agboola, P.O.; Dastgeer, G.; Shahid, M. Sol-gel assisted Ag doped $NiAl_2O_4$ nanomaterials and their nanocomposites with g-C3N4 nanosheets for the removal of organic effluents. *J. Alloys Compd.* **2022**, *902*, 163805. [CrossRef]
5. Rahman, A.; Aadil, M.; Akhtar, M.; Warsi, M.F.; Jamil, A.; Shakir, I.; Shahid, M. Magnetically recyclable $Ni_{1-x}Cd_xCe_yFe_{2-y}O_4$-rGO nanocomposite photocatalyst for visible light driven photocatalysis. *Ceram. Int.* **2020**, *46*, 13517–13526. [CrossRef]
6. Warsi, M.F.; Bashir, B.; Zulfiqar, S.; Aadil, M.; Khalid, M.U.; Agboola, P.O.; Shakir, I.; Yousuf, M.A.; Shahid, M. $Mn_{1-x}Cu_xO_2$/reduced graphene oxide nanocomposites: Synthesis, characterization, and evaluation of visible light mediated catalytic stud-ies. *Ceram. Int.* **2021**, *47*, 5044–5053. [CrossRef]
7. Stoyanova, M.; Christoskova, S. Catalytic degradation of methylene blue in aqueous solutions over Ni-and Co-oxide systems. *Open Chem.* **2011**, *9*, 1000–1007. [CrossRef]
8. Shukla, P.R.; Wang, S.; Sun, P.H.; Ang, H.M.; Tade, M. Activated carbon supported cobalt catalysts for advanced oxidation of organic contaminants in aqueous solution. *Appl. Catal. B Environ.* **2010**, *100*, 529–534. [CrossRef]
9. Macphee, D.E.; Rosenberg, D.; Skellern, M.G.; Wells, R.P.; Duffy, J.A.; Killham, K.S. A tungsten oxide-based photoelectrocata-lyst for degradation of environmental contaminants. *J. Solid State Electrochem.* **2011**, *15*, 99–103. [CrossRef]
10. Montini, T.; Gombac, V.; Hameed, A.; Felisari, L.; Adami, G.; Fornasiero, P. Synthesis, characterization and photocatalytic per-formance of transition metal tungstates. *Chem. Phys. Lett.* **2010**, *498*, 113–119. [CrossRef]
11. Ahmed, S.; Rasul, M.G.; Martens, W.; Brown, R.J.; Hashib, M.A. Advances in Heterogeneous Photocatalytic Degradation of Phenols and Dyes in Wastewater: A Review. *Water Air Soil Pollut.* **2011**, *215*, 3–29. [CrossRef]
12. Wang, Y.; Wang, Q.; Zhan, X.; Wang, F.; Safdar, M.; He, J. Visible light driven type II heterostructures and their enhanced pho-tocatalysis properties: A review. *Nanoscale* **2013**, *5*, 8326–8339. [CrossRef]
13. Shandilya, P.; Sambyal, S.; Sharma, R.; Mandyal, P.; Fang, B. Properties, optimized morphologies, and advanced strategies for photocatalytic applications of WO_3 based photocatalysts. *J. Hazard. Mater.* **2022**, *428*, 128218. [CrossRef] [PubMed]
14. Dai, G.; Yu, J.; Liu, G. Synthesis and Enhanced Visible-Light Photoelectrocatalytic Activity of p−n Junction $BiOI/TiO_2$ Nanotube Arrays. *J. Phys. Chem. C* **2011**, *115*, 7339–7346. [CrossRef]
15. Ma, D.; Xin, Y.; Gao, M.; Wu, J. Fabrication and photocatalytic properties of cationic and anionic S-doped TiO_2 nanofibers by electrospinning. *Appl. Catal. B Environ.* **2014**, *147*, 49–57. [CrossRef]
16. Kim, H.; Senthil, K.; Yong, K. Photoelectrochemical and photocatalytic properties of tungsten oxide nanorods grown by thermal evaporation. *Mater. Chem. Phys.* **2010**, *120*, 452–455. [CrossRef]
17. Bignozzi, C.A.; Caramori, S.; Cristino, V.; Argazzi, R.; Meda, L.; Tacca, A. Nanostructured photoelectrodes based on WO_3: Ap-plications to photooxidation of aqueous electrolytes. *Chem. Soc. Rev.* **2013**, *42*, 2228–2246. [CrossRef]

18. Aliannezhadi, M.; Minbashi, M.; Tuchin, V.V. Effect of laser intensity and exposure time on photothermal therapy with nanoparticles heated by a 793-nm diode laser and tissue optical clearing. *Quantum Electron.* **2018**, *48*, 559. [CrossRef]

19. Tian, Y.; Yi, W.; Bai, L.; Zhang, P.; Si, J.; Hou, X.; Deng, Y.; Hou, J. Lentinan in-situ coated tungsten oxide nanorods as a nano-therapeutic agent for low power density photothermal cancer therapy. *Int. J. Biol. Macromol.* **2019**, *137*, 904–911. [CrossRef]

20. Zheng, B.; Bai, Y.; Chen, H.; Pan, H.; Ji, W.; Gong, X.; Wu, X.; Wang, H.; Chang, J. Targeted delivery of tungsten oxide nanoparticles for multifunctional anti-tumor therapy via macrophages. *Biomater. Sci.* **2018**, *6*, 1379–1389. [CrossRef]

21. Dirany, N.; Arab, M.; Leroux, C.; Villain, S.; Madigou, V.; Gavarri, J.-R. Effect of WO$_3$ nanoparticles morphology on the cata-lytic properties. *Mater. Today Proc.* **2016**, *3*, 230–234. [CrossRef]

22. Fang, W.; Yang, Y.; Yu, H.; Dong, X.; Wang, T.; Wang, J.; Liu, Z.; Zhao, B.; Yang, M. One-step synthesis of flower-shaped WO$_3$ nanostructures for a high-sensitivity room-temperature NO x gas sensor. *RSC Adv.* **2016**, *6*, 106880–106886. [CrossRef]

23. Park, B.; Yong, K. Synthesis and characterization of tungsten oxide nanorods. *Surf. Rev. Lett.* **2005**, *12*, 745–748. [CrossRef]

24. Williamson, E.H.; Yao, N. Tungsten Oxide Nanorods: Synthesis, Characterization, and Application. In *Nanotechnology in Catalysis*; Springer: Berlin/Heidelberg, Germany, 2007; pp. 115–137.

25. Zappa, D.; Bertuna, A.; Comini, E.; Molinari, M.; Poli, N.; Sberveglieri, G. Tungsten oxide nanowires for chemical detection. *Anal. Methods* **2015**, *7*, 2203–2209. [CrossRef]

26. Park, S.-M.; Nah, Y.-C.; Nam, C. Effects of Hydrothermal Treatment Duration on Morphology of WO$_3$ Nanostructures. *J. Nanosci. Nanotechnol.* **2017**, *17*, 7719–7722. [CrossRef]

27. Sharma, P.; Minakshi, M.; Whale, J.; Jean-Fulcrand, A.; Garnweitner, G. Effect of the anionic counterpart: Molybdate vs. tung-state in energy storage for pseudo-capacitor applications. *Nanomaterials* **2021**, *11*, 580. [CrossRef]

28. Minakshi, M.; Mitchell, D.R.G.; Munnangi, A.R.; Barlow, A.J.; Fichtner, M. New insights into the electrochemistry of magnesium molybdate hierarchical architectures for high performance sodium devices. *Nanoscale* **2018**, *10*, 13277–13288. [CrossRef]

29. Hwang, S.K.; Kang, S.-M.; Rethinasabapathy, M.; Roh, C.; Huh, Y.S. MXene: An emerging two-dimensional layered material for removal of radioactive pollutants. *Chem. Eng. J.* **2020**, *397*, 125428. [CrossRef]

30. Aadil, M.; Zulfiqar, S.; Shahid, M.; Haider, S.; Shakir, I.; Warsi, M.F. Binder free mesoporous Ag-doped Co$_3$O$_4$ nanosheets with outstanding cyclic stability and rate capability for advanced supercapacitor applications. *J. Alloys Compd.* **2020**, *844*, 156062. [CrossRef]

31. Ali, A.; Aadil, M.; Rasheed, A.; Hameed, I.; Ajmal, S.; Shakir, I.; Warsi, M.F. Honeycomb like architectures of the Mo doped ZnS@Ni for high-performance asymmetric supercapacitors applications. *Synth. Met.* **2020**, *265*, 116408. [CrossRef]

32. Bashir, B.; Rahman, A.; Sabeeh, H.; Khan, M.A.; Aboud, M.F.A.; Warsi, M.F.; Shakir, I.; Agboola, P.O.; Shahid, M. Copper substi-tuted nickel ferrite nanoparticles anchored onto the graphene sheets as electrode materials for supercapacitors fabrication. *Ceram. Int.* **2019**, *45*, 6759–6766. [CrossRef]

33. Nazim, S.; Shahid, M.; Warsi, M.F.; Agboola, P.O.; Khan, M.A.; Shakir, I. Fabrication of efficient electrode material: Co$_x$Zn$_{1-x}$Fe$_2$O$_4$-graphene nano-heterostructures for high-performance supercapacitors. *Ceram. Int.* **2018**, *44*, 9616–9622. [CrossRef]

34. Sabeeh, H.; Zulfiqar, S.; Aadil, M.; Shahid, M.; Shakir, I.; Khan, M.A.; Warsi, M.F. Flake-like MoS2 nano-architecture and its nanocomposite with reduced Graphene Oxide for hybrid supercapacitors applications. *Ceram. Int.* **2020**, *46*, 21064–21072. [CrossRef]

35. Shaheen, N.; Aadil, M.; Zulfiqar, S.; Sabeeh, H.; Agboola, P.O.; Warsi, M.F.; Aboud, M.F.A.; Shakir, I. Fabrication of different conductive matrix supported binary metal oxides for supercapacitors applications. *Ceram. Int.* **2021**, *47*, 5273–5285. [CrossRef]

36. Shaheen, W.; Warsi, M.F.; Shahid, M.; Khan, M.A.; Asghar, M.; Ali, Z.; Sarfraz, M.; Anwar, H.; Nadeem, M.; Shakir, I. Carbon Coated MoO$_3$ Nanowires/Graphene oxide Ternary Nanocomposite for High-Performance Supercapacitors. *Electrochim. Acta* **2016**, *219*, 330–338. [CrossRef]

37. Warsi, M.F.; Shakir, I.; Shahid, M.; Sarfraz, M.; Nadeem, M.; Gilani, Z.A. Conformal Coating of Cobalt-Nickel Layered Double Hydroxides Nanoflakes on Carbon Fibers for High-performance Electrochemical Energy Storage Supercapacitor Devices. *Electrochim. Acta* **2014**, *135*, 513–518. [CrossRef]

38. Yousaf, S.; Aadil, M.; Zulfiqar, S.; Warsi, M.F.; Agboola, P.O.; Aboud, M.F.A.; Shakir, I. Hierarchically porous CuO micro-spheres and their r-GO based nanohybrids for electrochemical supercapacitors applications. *J. Mater. Res. Technol.* **2020**, *9*, 14158–14167. [CrossRef]

39. Alsafari, I.A.; Munir, S.; Zulfiqar, S.; Saif, M.S.; Warsi, M.F.; Shahid, M. Synthesis, characterization, photocatalytic and antibac-terial properties of copper Ferrite/MXene (CuFe$_2$O$_4$/Ti$_3$C$_2$) nanohybrids. *Ceram. Int.* **2021**, *47*, 28874–28883. [CrossRef]

40. Tahir, T.; Chaudhary, K.; Warsi, M.F.; Saif, M.S.; Alsafari, I.A.; Shakir, I.; Agboola, P.O.; Haider, S.; Zulfiqar, S. Synthesis of sponge like Gd^{3+} doped vanadium oxide/2D MXene composites for improved degradation of industrial effluents and pathogens. *Ceram. Int.* **2022**, *48*, 1969–1980. [CrossRef]

41. Wu, Z.-S.; Ren, W.; Wang, D.-W.; Li, F.; Liu, B.; Cheng, H.-M. High-energy MnO$_2$ nanowire/graphene and graphene asymmet-ric electrochemical capacitors. *ACS Nano* **2010**, *4*, 5835–5842. [CrossRef]

42. Mahmood, M.; Zulfiqar, S.; Warsi, M.F.; Aadil, M.; Shakir, I.; Haider, S.; Agboola, P.O.; Shahid, M. Nanostructured V$_2$O$_5$ and its nanohybrid with MXene as an efficient electrode material for electrochemical capacitor applications. *Ceram. Int.* **2021**, *48*, 2345–2354. [CrossRef]

43. Lai, W.-F.; Wong, W.-T. Use of graphene-based materials as carriers of bioactive agents. *Asian J. Pharm. Sci.* **2021**, *16*, 577–588. [CrossRef] [PubMed]

44. Barani, M.; Zeeshan, M.; Kalantar-Neyestanaki, D.; Farooq, M.A.; Rahdar, A.; Jha, N.K.; Sargazi, S.; Gupta, P.K.; Thakur, V.K. Nanomaterials in the Management of Gram-Negative Bacterial Infections. *Nanomaterials* **2021**, *11*, 2535. [CrossRef] [PubMed]

45. Soltani, M.D.; Meftahizadeh, H.; Barani, M.; Rahdar, A.; Hosseinikhah, S.M.; Hatami, M.; Ghorbanpour, M. Guar (Cyamopsis tetragonoloba L.) plant gum: From biological applications to advanced nanomedicine. *Int. J. Biol. Macromol.* **2021**, *193*, 1972–1985. [CrossRef]

46. Baldino, L.; Aragón, J.; Mendoza, G.; Irusta, S.; Cardea, S.; Reverchon, E. Production, characterization and testing of antibacteri-al PVA membranes loaded with HA-Ag$_3$PO$_4$ nanoparticles, produced by SC-CO$_2$ phase inversion. *J. Chem. Technol. Biotechnol.* **2019**, *94*, 98–108. [CrossRef]

47. Liao, G.; He, F.; Li, Q.; Zhong, L.; Zhao, R.; Che, H.; Gao, H.; Fang, B. Emerging graphitic carbon nitride-based materials for biomedical applications. *Prog. Mater. Sci.* **2020**, *112*, 100666. [CrossRef]

48. Chaudhary, K.; Shaheen, N.; Zulfiqar, S.; Sarwar, M.I.; Suleman, M.; Agboola, P.O.; Shakir, I.; Warsi, M.F. Binary WO$_3$-ZnO nanostructures supported rGO ternary nanocomposite for visible light driven photocatalytic degradation of methylene blue. *Synth. Met.* **2020**, *269*, 116526. [CrossRef]

49. Tehrani, F.S.; Ahmadian, H.R.; Aliannezhadi, M. Hydrothermal synthesis and characterization of WO$_3$ nanostructures: Effect of reaction time. *Mater. Res. Express* **2020**, *7*, 015911. [CrossRef]

50. Mu, W.; Yu, Q.; Li, X.; Wei, H.; Jian, Y. Hydrothermal synthesis of WO$_3$ nanowires in the presence of guanidine sulfate and its photocatalytic activity. *J. Wuhan Univ. Technol. Sci. Ed.* **2016**, *31*, 731–735. [CrossRef]

51. Balzer, R.; Drago, V.; Schreiner, W.H.; Probst, L.F.D. Synthesis and Structure-Activity Relationship of a WO$_3$ Catalyst for the Total Oxidation of BTX. *J. Braz. Chem. Soc.* **2014**. [CrossRef]

52. Naguib, M.; Kurtoglu, M.; Presser, V.; Lu, J.; Niu, J.; Heon, M.; Hultman, L.; Gogotsi, Y.; Barsoum, M.W. Two-dimensional nano-crystals produced by exfoliation of Ti$_3$AlC$_2$. *Adv. Mater.* **2011**, *23*, 4248–4253. [CrossRef] [PubMed]

53. Rajavel, K.; Ke, T.; Yang, K.; Lin, D. Condition optimization for exfoliation of two-*dimensional* titanium carbide (Ti$_3$C$_2$Tx). *Nanotechnology* **2018**, *29*, 095605. [CrossRef] [PubMed]

54. Scheibe, B.; Kupka, V.; Peplińska, B.; Jarek, M.; Tadyszak, K. The Influence of Oxygen Concentration during MAX Phases (Ti$_3$AlC$_2$) Preparation on the α-Al$_2$O$_3$ Microparticles Content and Specific Surface Area of Multilayered MXenes (Ti$_3$C$_2$Tx). *Materials* **2019**, *12*, 353. [CrossRef] [PubMed]

55. Chen, L.; Shi, X.; Yu, N.; Zhang, X.; Du, X.; Lin, J. Measurement and Analysis of Thermal Conductivity of Ti$_3$C$_2$Tx MXene Films. *Materials* **2018**, *11*, 1701. [CrossRef]

56. Chang, F.; Li, C.; Yang, J.; Tang, H.; Xue, M. Synthesis of a new graphene-like transition metal carbide by de-intercalating Ti$_3$AlC$_2$. *Mater. Lett.* **2013**, *109*, 295–298. [CrossRef]

57. Munir, S.; Rasheed, A.; Rasheed, T.; Ayman, I.; Ajmal, S.; Rehman, A.; Shakir, I.; Agboola, P.O.; Warsi, M.F. Exploring the Influ-ence of Critical Parameters for the Effective Synthesis of High-Quality 2D MXene. *ACS Omega* **2020**, *5*, 26845–26854. [CrossRef] [PubMed]

58. Aadil, M.; Zulfiqar, S.; Sabeeh, H.; Warsi, M.F.; Shahid, M.; Alsafari, I.A.; Shakir, I. Enhanced electrochemical energy storage properties of carbon coated Co$_3$O$_4$ nanoparticles-reduced graphene oxide ternary nano-hybrids. *Ceram. Int.* **2020**, *46*, 17836–17845. [CrossRef]

59. Patterson, A.L. The Scherrer Formula for X-ray Particle Size Determination. *Phys. Rev. (Ser. I)* **1939**, *56*, 978–982. [CrossRef]

60. Mahmood, M.; Rasheed, A.; Ayman, I.; Rasheed, T.; Munir, S.; Ajmal, S.; Agboola, P.O.; Warsi, M.F.; Shahid, M. Synthesis of Ul-trathin MnO$_2$ Nanowire-Intercalated 2D-MXenes for High-Performance Hybrid Supercapacitors. *Energy Fuels* **2021**, *35*, 3469–3478. [CrossRef]

61. Herrmann, J.-M. Water Treatment by Heterogeneous Photocatalysis. In *Environmental Catalysis*; World Scientific: Singapore, 1999; pp. 171–194. [CrossRef]

62. Karimi-Maleh, H.; Kumar, B.G.; Rajendran, S.; Qin, J.; Vadivel, S.; Durgalakshmi, D.; Gracia, F.; Soto-Moscoso, M.; Orooji, Y.; Karimi, F. Tuning of metal oxides photocatalytic performance using Ag nanoparticles integration. *J. Mol. Liq.* **2020**, *314*, 113588. [CrossRef]

63. Zhang, J.; Ding, E.; Xu, S.; Li, Z.; Fakhri, A.; Gupta, V.K. Production of metal oxides nanoparticles based on poly-alanine/chitosan/reduced graphene oxide for photocatalysis degradation, anti-pathogenic bacterial and antioxidant studies. *Int. J. Biol. Macromol.* **2020**, *164*, 1584–1591. [CrossRef] [PubMed]

64. Karthik, K.; Dhanuskodi, S.; Gobinath, C.; Prabukumar, S.; Sivaramakrishnan, S. Photocatalytic and antibacterial activities of hydrothermally prepared CdO nanoparticles. *J. Mater. Sci. Mater. Electron.* **2017**, *28*, 11420–11429. [CrossRef]

65. Karthik, K.; Dhanuskodi, S.; Gobinath, C.; Prabukumar, S.; Sivaramakrishnan, S. Multifunctional properties of CdO nanostructures Synthesised through microwave assisted hydrothermal method. *Mater. Res. Innov.* **2019**, *23*, 310–318. [CrossRef]

66. Karthik, K.; Revathi, V.; Tatarchuk, T. Microwave-assisted green synthesis of SnO$_2$ nanoparticles and their optical and pho-tocatalytic properties. *Mol. Cryst. Liq. Cryst.* **2018**, *671*, 17–23. [CrossRef]

67. Revathia, V.; Karthikb, K. Physico-chemical Properties and Antibacterial Activity of Hexakis (thiocarbamide) Nickel (II). *Acta Part A* **2007**, *66*, 707.

68. Karthik, K.; Naik, M.M.; Shashank, M.; Vinuth, M.; Revathi, V. Microwave-Assisted ZrO$_2$ Nanoparticles and Its Photocatalytic and Antibacterial Studies. *J. Clust. Sci.* **2019**, *30*, 311–318. [CrossRef]

69.   Karthik, K.; Dhanuskodi, S.; Gobinath, C.; Prabukumar, S.; Sivaramakrishnan, S. Fabrication of MgO nanostructures and its efficient photocatalytic, antibacterial and anticancer performance. *J. Photochem. Photobiol. B Biol.* **2019**, *190*, 8–20. [CrossRef]

70.   Karthik, K.; Shashank, M.; Revathi, V.; Tatarchuk, T. Facile microwave-assisted green synthesis of NiO nanoparticles from Andrographis paniculata leaf extract and evaluation of their photocatalytic and anticancer activities. *Mol. Cryst. Liq. Cryst.* **2018**, *673*, 70–80. [CrossRef]

71.   Karthik, K.; Dhanuskodi, S.; Gobinath, C.; Prabukumar, S.; Sivaramakrishnan, S. Multifunctional properties of microwave assisted CdO–NiO–ZnO mixed metal oxide nanocomposite: Enhanced photocatalytic and antibacterial activities. *J. Mater. Sci. Mater. Electron.* **2018**, *29*, 5459–5471. [CrossRef]

72.   Revathi, V.; Karthik, K. Microwave assisted CdO–ZnO–MgO nanocomposite and its photocatalytic and antibacterial studies. *J. Mater. Sci. Mater. Electron.* **2018**, *29*, 18519–18530. [CrossRef]

73.   Karthik, K.; Dhanuskodi, S.; Gobinath, C.; Prabukumar, S.; Sivaramakrishnan, S. Ultrasonic-assisted CdO–MgO nanocompo-site for multifunctional applications. *Mater. Technol.* **2019**, *34*, 403–414. [CrossRef]

74.   Houas, A.; Lachheb, H.; Ksibi, M.; Elaloui, E.; Guillard, C.; Herrmann, J.-M. Photocatalytic degradation pathway of methylene blue in water. *Appl. Catal. B Environ.* **2001**, *31*, 145–157. [CrossRef]

75.   Yang, X.; Shao, H.; Liu, W.; Gu, W.; Shu, X.; Mo, Y.; Chen, X.; Zhang, Q.; Jiang, M. Endoplasmic reticulum stress and oxidative stress are involved in ZnO nanoparticle-induced hepatotoxicity. *Toxicol. Lett.* **2015**, *234*, 40–49. [CrossRef] [PubMed]

76.   Wen, L.; Chen, L.; Zheng, S.; Zeng, J.; Duan, G.; Wang, Y.; Wang, G.; Chai, Z.; Li, Z.; Gao, M. Ultrasmall Biocompatible WO_{3-x} Nanodots for Multi-Modality Imaging and Combined Therapy of Cancers. *Adv. Mater.* **2016**, *28*, 5072–5079. [CrossRef]

77.   Akhavan, O.; Ghaderi, E. Toxicity of graphene and graphene oxide nanowalls against bacteria. *ACS Nano* **2010**, *4*, 5731–5736. [CrossRef]

78.   Niu, A.; Han, Y.; Wu, J.; Yu, N.; Xu, Q. Synthesis of One-Dimensional Carbon Nanomaterials Wrapped by Silver Nanoparticles and Their Antibacterial Behavior. *J. Phys. Chem. C* **2010**, *114*, 12728–12735. [CrossRef]

79.   Jagadeeshan, S.; Parsanathan, R. Nano-Metal Oxides for Antibacterial Activity. In *Advanced Nanostructured Materials for Environmental Remediation*; Springer: Berlin/Heidelberg, Germany, 2019; pp. 59–90.